Nanoscale

PAPER

View Article Online
View Journal | View Issue

Cite this: *Nanoscale*, 2026, **18**, 5918

Biosynthesized iron oxide nanoparticles using *Trichoderma harzianum* with applications for phytopathogen control

Erika Armenta-Jaime, †[a,e] Ángeles Alitzel Rivera Román,†[b] América R. Vázquez-Olmos, [c] Velma Beri Kimbi Yaah, [d] Satu Ojala, [e] Oscar Arce Cervantes, [b] Andrés Galdámez-Martínez *[d] and Silvia Armenta *[b]

In the pursuit of a sustainable transition toward green synthesis, the biological production of nanomaterials emerges as an attractive alternative for generating nanomaterials with controlled physicochemical properties. In this work, Fe-based nanostructures were biosynthesized using *Trichoderma harzianum* with iron precursor concentrations of 5 mM (Fe5) and 10 mM (Fe10), followed by thermal treatment. SEM, AFM, and TEM analyses revealed that precursor concentration governs particle size and aggregation, while annealing drives the phase evolution from Fe_3O_4 based composition in the as-synthesized nanomaterials to a crystalline α-Fe_2O_3 phase, as confirmed by XRD and XPS. These techniques further indicate that this transformation is associated with the removal of capping biomolecules and the oxidation of Fe(II) to Fe(III). Biologically, Fe5 and Fe10 acted as potent biostimulants, enhancing *T. harzianum* growth, sporulation, and pigmentation without inhibition. Dual-culture assays demonstrated that both materials significantly increased the fungus's antagonistic activity against *Fusarium oxysporum*, *Fusarium verticillioides*, and *Phytophthora infestans*. These results highlight the potential of biosynthesized Fe oxide nanoparticles as dual-function platforms that couple nanotechnology and biological control for sustainable crop protection.

Received 10th November 2025,
Accepted 10th February 2026

DOI: 10.1039/d5nr04745e

rsc.li/nanoscale

1. Introduction

Global agriculture faces ongoing threats from phytopathogens, which cause significant losses in both crop yield and quality worldwide. Conventional control strategies overwhelmingly depend on chemical pesticides; although effective, these methods have drawbacks including adverse environmental and health impacts, and the risk of selecting for resistant pathogen strains. Consequently, there is a pressing need for sustainable, eco-friendly alternatives that preserve both food security and ecosystem integrity.

Nanotechnology offers one such avenue: nanomaterials with antimicrobial activity are emerging as powerful tools for phytopathogen control. Among them, iron oxide nanostructures (notably Fe_2O_3 and Fe_3O_4) are especially attractive due to their favorable physicochemical properties, cost-effectiveness, biocompatibility, and their dual functionality, acting both as antimicrobial agents and micronutrients critical for plant growth. Several recent studies underline these potentials. For example, Hasan *et al.* reported that biosynthesized iron oxide nanoparticles (NPs) exhibit peroxidase-like activity with low cytotoxicity, suggesting suitability for agricultural and environmental applications.[1] On the other hand, Fatih *et al.* demonstrated that green-synthesized α-Fe_2O_3 nanoparticles have strong antibacterial, anti-biofilm, and anti-virulence effects against pathogenic bacteria, underscoring their growing relevance as biocontrol agents.[2]

Despite these advantages, many methods for synthesizing iron oxide nanomaterials rely on physical and chemical processes that are often energy-intensive, produce hazardous by-products, or require harsh conditions. In contrast, green or biological synthesis methods are gaining interest, permitting production under milder conditions, often yielding particles with natural capping agents and enhanced environmental compatibility. Fungi are excellent candidates for this purpose, owing to their robust metal tolerance and secretion of reductive metabolites (enzymes, organic acids, *etc.*) that mediate nanoparticle formation.[3] Recently, Gallo *et al.*[4] revealed multiple oxidoreductase enzymes that appear to play key roles in

[a]*Facultad de Química, Universidad Nacional Autónoma de México, México City, 04510, Mexico*
[b]*Instituto de Ciencias Agropecuarias, Universidad Autónoma del Estado de Hidalgo, 43600 Tulancingo, Hidalgo, Mexico. E-mail: silvia_armenta@uaeh.edu.mx*
[c]*Instituto de Ciencias Aplicadas y Tecnología, Universidad Nacional Autónoma de México, Circuito Exterior S/N, 04510 Ciudad de México, Mexico*
[d]*Nano and Molecular Systems Research Unit, University of Oulu, 90014 Oulu, Finland. E-mail: andres.galdamezmartinez@oulu.fi*
[e]*Environmental and Chemical Engineering, Faculty of Technology, University of Oulu, Oulu, Finland*
† Equal contribution

the biosynthesis of zinc/iron oxide nanoparticles, demonstrating how fungal metabolism can be harnessed to produce NPs with controlled morphology and composition.

Beyond synthesis, fungi such as species in the genus *Trichoderma* are well-known for their biocontrol capabilities. They produce a variety of secondary metabolites, volatile compounds, hydrolytic enzymes, and display antagonism against many phytopathogens. Reviews have summarized recent advances in using *Trichoderma* both for direct pathogen suppression and for plant growth stimulation.[5] Recent work also indicates that combining iron oxide nanoparticles with *Trichoderma* sp. can enhance plant responses under stress (*e.g.* drought) or improve resistance to specific pathogens (for example *Fusarium* wilt), suggesting a synergistic benefit of integrating NPs with fungal agents. Shao *et al.* showed that *T. harzianum* not only improves plant growth in calcareous soils, but its interaction with soil microbial communities enhances iron mobilization, a finding that could complement nanoparticle-based iron delivery strategies.[6]

Therefore, this study aims to synthesize iron oxide nanoparticles *via Trichoderma harzianum*, controlling their morphological, compositional, and optical properties, and to assess their potential both to stimulate *T. harzianum* growth and to enhance its antagonistic activity against agriculturally relevant phytopathogens. By uniting green nanoparticle synthesis with fungal biocontrol into a single platform, we propose a synergistic biotechnological strategy that may offer more effective, less chemically dependent disease management in agriculture.

2. Materials and methods

2.1 *Trichoderma harzianum* biomass obtention

Trichoderma harzianum was grown on Potato Dextrose Agar (PDA) at 25 °C for one week. *T. harzianum* inoculum was prepared by adding 10 mL of sterile distilled water on PDA, followed by removing the mycelium. To produce fungal biomass, 100 mL of liquid medium composed of peptone (32.6%), sodium chloride (16.3%), disodium phosphate (11.4%), monopotassium phosphate (4.9%), magnesium chloride (0.3%), yeast extract (2.0%), and dextrose (32.6%), were inoculated with 1 mL of inoculum and cultured for 7 days at 25 °C, 100 rpm. After, the cultures underwent centrifugation at 6500 rpm, 15 °C for 15 min. The supernatant was removed, and the resulting biomass was transferred to a flask containing 100 mL of sterile distilled water, then incubated at 25 °C, 100 rpm for 72 h. Subsequently, the extract was obtained through centrifugation at 8000 rpm, 15 °C for 15 min.

2.2 Nanomaterials fungal biosynthesis

Fungal filtrates were placed on an orbital shaker at 100 rpm to facilitate the addition of ferrous acetate salt ($Fe(C_2H_3O_2)_2$). Controlled dropwise addition of a 500 mM $Fe(C_2H_3O_2)_2$ solution was performed into 100 mL of fungal extract until reaching final concentrations of 5 mM and 10 mM, herein referred to as Fe5 and Fe10, respectively. The cultures were incubated at 25 °C and 100 rpm for 72 h. Following incubation, each flask was transferred into 50 mL centrifuge tubes and centrifuged at 12 000 rpm and 15 °C for 15 min. Supernatants were discarded, and the resulting pellets (Fe5 and Fe10) were oven-dried at 60 °C for 24 h. The dried materials were finely ground in an agate mortar to obtain biosynthesized iron oxide nanoparticles. Additionally, to remove capping agents and promote crystallization, selected Fe5 and Fe10 samples were thermally treated at 600 °C for 2 h in a Nabertherm LT 3/11 muffle furnace under ambient air (oxygen partial pressure ≈160 mmHg), followed by natural cooling to room temperature; the resulting samples were labeled Fe5HT and Fe10HT.

2.3 Material characterization

The morphology of the synthesized materials was examined using secondary electron images (SEI) acquired with a Zeiss Ultra Plus field-emission scanning electron microscope (FESEM). Topography and surface roughness features of the samples were evaluated by atomic force microscopy (AFM) using a Nanosurf FlexAFM system operating in tapping mode. JEOL JEM-2200FS EFTEM/STEM instrument was used to perform transmission electron microscopy (TEM), selected area electron diffraction (SAED), scanning transmission electron microscopy (STEM) and energy-dispersive X-ray spectroscopy (EDS) elemental mappings measurements. Structural characterization was carried out using X-ray diffraction (XRD). As-synthesized samples were measured using a Rigaku Miniflex diffractometer (600 W, Co K_α radiation, λ = 1.7909 Å, 2θ = 20–75°, step size 0.02°), while heat-treated samples were analyzed using a Rigaku SmartLab diffractometer (9 kW, Co K_α radiation, λ = 1.7909 Å, 2θ = 20–75°, step size 0.02°). All XRD experiments were performed using a Co K_β filter and zero background holders. X-ray photoelectron spectroscopy (XPS) measurements were performed using a Thermo Scientific ESCALAB 250Xi system (Al Kα source, $h\nu$ = 1486.6 eV), collecting survey spectra over a binding energy range of 0–1350 eV to assess the elemental composition of the samples. High-resolution XPS spectra were deconvoluted using the Avantage software package. A combination of Gaussian (G) and Lorentzian (L) curves with an L/G mix product of 30.0% were employed together with a Shirley background. UV-Vis-NIR spectroscopy measurements were used to assess the optical properties of the biosynthesized materials. Absorbance and diffuse reflectance spectra (DRS) were acquired over the 190–1400 nm range using a Shimadzu UV-2600 spectrophotometer equipped with an ISR-2600 Plus integrating sphere. The optical band gaps of the synthesized samples were determined using Tauc plot fitting. Finally, to evaluate functional groups' presence, Fourier-transform infrared (FTIR) spectroscopy was performed using a Bruker Vertex v80.

2.4 Stimulatory effect of biosynthesized iron oxide nanoparticles on the growth of *Trichoderma harzianum*

The biosynthesized Fe5 and Fe10 nanoparticles were incorporated into potato dextrose agar (PDA) at a concentration of 100 ppm. The medium was homogenized for 30 min before

dispensing 10 mL into 50 mm Petri dishes. A mycelial plug of *T. harzianum* was placed at the center of each plate and incubated at 28 °C for seven days. In addition, the post-synthesis viability of *T. harzianum* was evaluated to determine whether the fungus remained active after participating in the nanoparticle biosynthesis. For this purpose, 10 mL of sterile distilled water was added to the Fe10 pellet and homogenized for 30 min. The resulting suspension (*T. harzianum* + Fe10) was incorporated as a plug into PDA medium to assess whether mycelial growth could originate from reproductive structures attached to Fe10 surface. Plates inoculated with *T. harzianum* + Fe10 suspension and control plates containing only *T. harzianum* were incubated under identical conditions, and their radial growth and mycelial morphology were monitored at 1, 2, 3, 4, 6, and 7 days.

2.5 Antagonistic activity of *Trichoderma harzianum*

The antagonistic capacity of *T. harzianum* was assessed against *Fusarium oxysporum*, *Fusarium verticillioides*, and *Phytophthora infestans*. Biosynthesized Fe5 and Fe10 nanoparticles were incorporated into PDA at a concentration of 100 ppm and homogenized for 5 min. Approximately 10 mL of medium was poured into 50 mm Petri dishes. A pathogen mycelial plug was placed at one edge of each plate; after two days, a plug of *T. harzianum* was placed at the opposite edge. Plates were incubated at 28 °C for seven days. Growth dynamics and mycelial morphology were evaluated at 1, 3, 7, 10, and 13 days. The antagonistic degree was determined for each treatment following the scale proposed by Bell *et al.*[7] (Table 1).

3. Results and discussion

The morphological characteristics of the biosynthesized iron oxide samples were examined *via* scanning electron microscopy (SEM). Fig. 1(a and b) shows the SEM images of the materials synthesized with 5 mM and 10 mM iron precursor concentrations, denoted as Fe5 and Fe10 respectively. For imaging, the powdered dried Fe5 and Fe10 samples were directly sprinkled onto carbon tape and coated with a thin conductive sputtered platinum layer. No additional processing steps, such as sonication, dispersion, and drop-casting, were used to isolate smaller structures. SEI images reveal the formation of irregular shaped microstructures, with average sizes of 6.0 ± 3.0 μm for Fe5 and 10 ± 3 μm for Fe10. In both cases, the size distributions extended up to 30 μm (see magnified images in SI, SI 1). These results indicate a direct relation between precursor concentration and microstructure size, pointing out that higher precursor concentrations lead to the formation of larger structures.

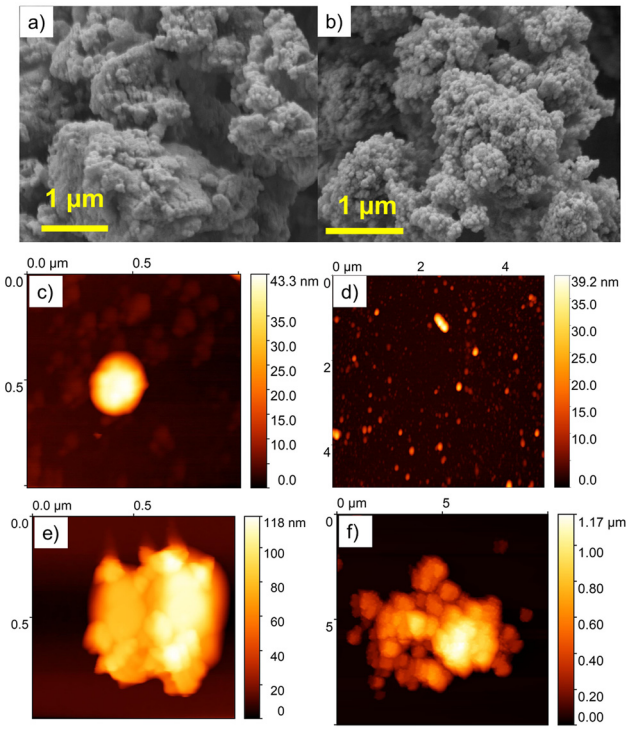

Fig. 1 (a and b) Secondary electron images (SEI) of the biosynthesized iron oxide nanomaterials: (a) Fe5 (5 mM) and (b) Fe10 (10 mM), acquired using secondary electron detectors. (c–f) Atomic force microscopy (AFM) images of Fe5 (c and d) and Fe10 (e and f) samples.

Furthermore, both samples exhibit surface decoration with quasi-spherical nanoparticles (NPs). In the Fe5 sample, these NPs had an average diameter of 159 ± 9 nm, while slightly smaller structures averaging 140 ± 8 nm were observed for Fe10. These values were determined through statistical analysis of multiple SEM micrographs using ImageJ software. The measured size distributions were fitted to log–normal distributions, as presented in SI 2. Notably, while precursor concentration appears to have limited influence on the size of individual NPs, it significantly affects their surface coverage. The Fe10 sample displays a more densely decorated microstructure surface, with virtually no bare regions, whereas the Fe5 sample still presents areas devoid of nanoparticles decoration. This observation suggests that precursor concentration mainly governs the density of microstructure surface coverage rather than the size of the NPs.

To gain further insight into surface topography, atomic force microscopy (AFM) images of Fe5 and Fe10 samples were

Table 1 Antagonism scale by Bell *et al.*[7] for determining antagonistic ability of *Trichoderma* sp.

Degree	Description
1	*Trichoderma* sp. completely overgrew the pathogen and colonized the entire plate surface.
2	*Trichoderma* sp. colonized more than two-thirds of the plate surface.
3	*Trichoderma* sp. and the pathogen each colonized half of the plate surface, with no dominance observed.
4	The pathogen colonized at least two-thirds of the plate surface and resisted invasion by *Trichoderma* sp.
5	The pathogen completely overgrew *Trichoderma* sp. and colonized the entire plate surface.

attained. For AFM imaging, powdered samples were dispersed in ethanol (1 mg mL^{-1}), sonicated for 10 min, and drop-casted onto crystalline silicon substrates. Fig. 1(c–f) shows the AFM micrographs of the synthesized samples in tapping operating mode. The images processing (*i.e.* background subtraction, height calibration, and row alignment *via* mean-line correction) was carried out using Gwyddion software.

For Fe5 sample, analysis of Fig. 1(d) using the particle analysis tool in ImageJ (SI 3) revealed an average particle diameter of 108 ± 7 nm. The nanostructures exhibited quasi-spherical morphology with good homogeneity across the substrate, aligning well with the nanoscale surface features previously observed in SEM. This suggests that the sonication process effectively removes surface-bound nanostructures from the Fe5 microstructures.

In contrast, the Fe10 sample showed noticeably different behavior. Despite undergoing identical dispersion and sonication conditions, the Fe10 material largely retained its microstructure form with attached nanoparticles exhibiting higher agglomeration compared to the Fe5 sample. For Fe10 sample, ImageJ analysis indicated the presence of larger agglomerates with sizes from 8.49 to 0.69 μm. Surface roughness analysis further supports these observations. Root mean square (RMS) roughness values (S_q) calculated from AFM measurements were 11.3 ± 6.1 nm for Fe5 and 96.9 ± 51.7 nm for Fe10, respectively. These values indicate a pronounced increase in surface roughness for the Fe10 sample as result of higher nanostructured decoration, consistent with the morphological differences observed through SEM. As we can see, using 10 mM of iron precursor concentration gives rise to higher yield of nanostructures but accompanied by higher agglomeration.

Since the 10 mM precursor concentration yielded a higher amount of nanostructured material, this condition was selected for further characterization using transmission electron microscopy (TEM). To prepare the samples, we employed a sonication procedure for 10 minutes in ethanol followed by drop casting into carbon grids. Fig. 2(a-b) shows the obtained micrography for Fe10 sample, where the formation of heterogeneous granular agglomerated structures with sizes of (193 ± 129) nm can be observed, which agrees with both AFM and SEM results. By measuring the peripheral regions, we could observe small nanoparticles (NPs) of around 19 ± 11 nm agglomerating into larger nanostructures. Agglomeration has been reported as a typical mechanism to reduce surface energy in nanostructured systems.[8] Selected area electron diffraction (SAED) patterns (see Fig. 2(b)) showed diffuse rings indicating an amorphous nature for the Fe10 sample.

To increase crystallinity, the samples (Fe5 and Fe10) were subjected to post-synthesis heat treatment (HT) at 600 °C for 2 hours in air atmosphere (the samples were labeled as Fe5HT and Fe10HT, respectively). Fig. 2(c and d) shows the TEM images of Fe10HT sample, where the formation of nanoparticles (approximately 13 ± 6 nm) is more clearly observed in the peripheral region of the microstructures, compared to Fe10 sample. However, despite the annealing process, the

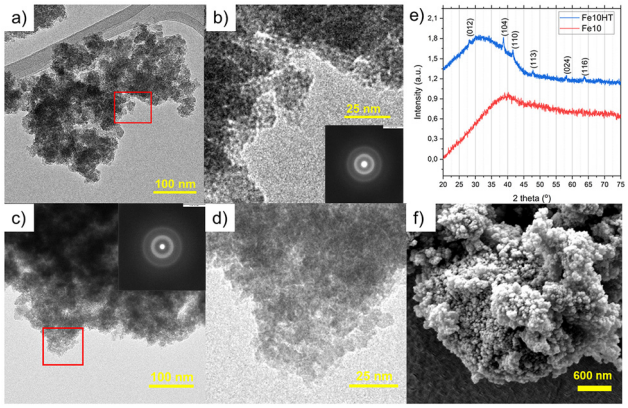

Fig. 2 (a and b) Transmission electron microscopy (TEM) images and corresponding selected area electron diffraction (SAED) patterns for Fe10 (a and b) and Fe10HT samples (c and d). (e) X-ray diffraction (XRD) patterns of the Fe10 and Fe10HT, showing the presence of α-Fe_2O_3 in the thermally treated sample. (f) SEM micrograph of Fe10HT shows no significant changes in morphology due to heat treatment process.

SAED patterns still exhibit diffuse rings, which are attributed to the amorphous nature of the selected area given the nanoparticles sizes surrounded by organic compounds (capping agents), along with dark, electron-opaque regions ascribed to nanoparticles' agglomeration and sintering effects. Nevertheless, SAED patterns of Fe5HT show defined spots that were successfully indexed to the Fe_2O_3 structure (zone axis −341) using the CrysTBox software,[9] as shown in SI 4.

Subsequently, X-ray diffractograms were measured to determine the general structural nature of the Fe samples before and after HT. The Fe10 sample diffractogram (Fig. 2(e)) exhibits no well-defined diffraction peaks, confirming its amorphous structure. In contrast, the Fe10HT sample (blue line) showed distinct diffraction peaks at 28.1°, 38.7°, 41.6°, 47.9°, 58.0°, 63.7° and 76.0° attributed to the (012), (104), (110), (113), (024), (116) and (300) of the α-Fe_2O_3 phase (hematite), in agreement with the ICDD reference PDF-5+ (04-015-6945), with a figure of merit of 0.621. These results indicate that the calcination process promotes a structural rearrangement of iron oxide into its thermodynamically stable α-phase. Average crystallite size of (11 ± 5) nm was determined for Fe10HT sample using the Scherrer equation.[10] XRD patterns of Fe5 and Fe5HT (SI 4) show limited crystallinity for the materials biosynthesized with a 5 mM precursor concentration.

In addition, to evaluate the impact of the annealing process on the morphological features of the samples, SEM images were acquired for Fe5HT (SI 5) and Fe10HT (Fig. 2(f)). For the Fe10HT sample, a statistical analysis of the nanostructure's coverage revealed average sizes of 129 ± 8 nm, respectively. No significant morphological differences were observed after the post-treatment process, which suggests that the sample remained essentially unchanged.

Since diffraction-based techniques allow structural identification only for materials with sufficient long-range crystalline order, the analysis of the biosynthesized samples prior to

thermal treatment was complemented by spectroscopic techniques, which enable confirmation of chemical composition and iron oxidation states even in amorphous materials. Elemental characterization was carried out using energy-dispersive X-ray spectroscopy (EDS) coupled with scanning transmission electron microscopy (STEM). The full compositional maps for both Fe10 and Fe10HT and EDS spectra are presented in Fig. 3. The EDS spectra confirm the presence of C, N, O, Na, P, K, and Fe (Fig. 3(a and c); Table S1), being Fe, O, and P the most abundant elements in both samples. These elements reflect the chemical composition of the biological capping derived from *Trichoderma harzianum*, employed in the synthesis process. All elements exhibited a homogeneous distribution throughout both samples surfaces (for Fe10 and Fe10HT) with slight variations on their concentration.

Based on the elements with higher concentration in the samples (*i.e.* Fe, O, and P), RGB overlay maps were constructed, assigning Fe to red, O to green, and P to blue channels (SI 6). As shown in SI 6(c), regions with white coloration indicate similar composition of the three elements (Fe10 sample). On the other hand, RGB maps for Fe10HT (see SI 6(d)) display a predominantly yellow hue, reflecting the major presence of Fe and O (red and green channels) with reduced P signal. This shift suggests that thermal treatment facilitates the removal of phosphorus through its oxidation to form volatile compounds, promoting the formation of purer Fe oxide nanostructures. The presence of P in the samples originates from the organic matter presented in the caping agents. The decrease in relative organic content can be also corroborated by a decrease in intensity of the CK_α signal after calcination, as shown in Fig. 3(b–d). The iron content and batch-to-batch reproducibility of the biosynthesized materials were evaluated by TEM-EDS and SEM-EDS analyses, with quantitative results summarized in Table S2 (SI 7).

To characterize in more detail the composition and the chemical environments of the biosynthesized samples, X-ray photoelectron spectroscopy (XPS) measurements were carried out for Fe10 and Fe10HT samples. All the measurements were calibrated using the C 1s orbital (284.8 eV) as reference.[11] The survey spectra (0–1350 eV binding energy) are shown in Fig. 4(a). For the Fe10 sample, characteristic peaks associated with the following elemental orbitals and Auger emissions were identified: O 2s (22.1 eV), Fe 3p (55.0 eV), Na 2s (63.4 eV), Fe 3s (93.0 eV), P 2p (132.0 eV), P 2s (189.8 eV), C 1s (284.8 eV), N 1s (398.8 eV), O 1s (529.9 eV), Fe 2p3 (709.9 eV), Fe 2p1 (723.1 eV), Fe LM1 (771.4 eV), Fe LM2 (783.3 eV), Fe LM3 (807.6 eV), Fe 2s (842.3 eV), Fe LM7 (924.2 eV), O KL1 (975.3 eV), O KL2 (994.9 eV) and C KL1 (1220.6 eV). In contrast, the Fe10HT sample exhibited a similar set of peaks, with the notable absence of the N 1s and C KLL signals as well as a significant decrease of the C 1s peak. The thermal treatment reduces the contribution from biologically derived elements (particularly carbon and nitrogen) while enhancing the signals associated with iron and oxygen, suggesting partial decomposition of organic material and probably delivered as CO_2, NO_x and PO_x molecules.[12]

To profound more on the chemical environments of each element, high resolution XPS (HRXPS) spectra measurements were performed for the C 1s, O 1s and Fe 3p orbitals (Fig. 4(b and c)). Deconvolution using Gaussian/Lorentzian curves of the C 1s spectra for Fe10 sample allows us to identify signals in 284.7 eV, 286.1 eV and 288.1 eV that can be assigned to C–C, C–O–C and C═O bonds coming from the organic capping

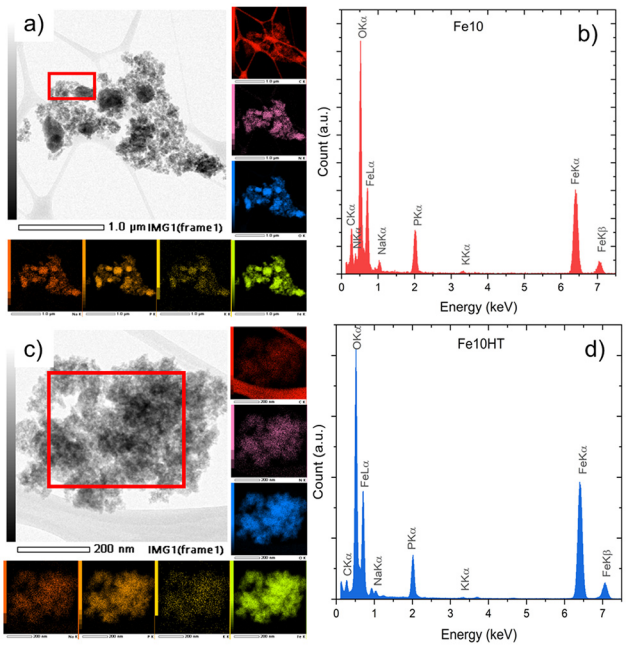

Fig. 3 Elemental mapping by EDS in STEM images of Fe10 (a and b) and Fe10HT (c and d) nanostructures. EDS spectra showing characteristic X-ray emissions of C, N, O, Na, P and Fe. The spectrums were obtained from the highlighted areas.

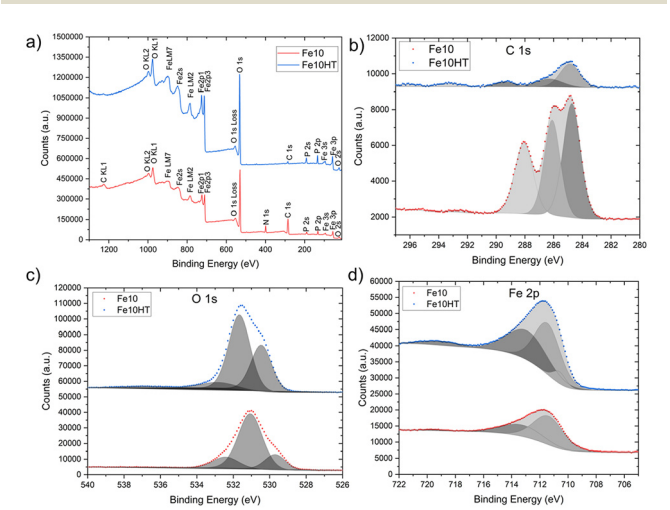

Fig. 4 X-ray photoelectron spectroscopy (XPS) spectra of Fe10 and Fe10HT samples. (a) Survey spectra recorded in the binding energy range from 1350 to 0 eV. (b–d) High-resolution XPS spectra corresponding to (b) C 1s, (c) O 1s and (d) Fe 2p orbitals.

layer.[13] On the other hand, for Fe10HT, the peaks assigned to the bonds C–O–C and C═O (286.3 eV and 289. 4 eV) decrease in intensity in comparison with the C–C peak (284.9 eV),[13] confirming still the presence of organic matter after the heat treatment. In addition, we observed the presence of potassium doublet K 2p in 293.3 eV (K $2p_{3/2}$) and 296.2 eV (K $2p_{1/2}$), which overlaps with C signals, and agree with the EDS results.[14] Overall, the unnormalized spectra from Fig. 4(b) shows a clear decrease in C 1s intensity as a result of the annealing process.

Additional O 1s HRXPS were acquired for Fe10 and Fe10HT samples. The deconvolution process adjusts with three peaks at 529.7 eV, 531.1 eV, and 532.4 eV (for Fe10) which have been attributed to metal oxide signal, C═O and C–O respectively,[15–17] confirming the obtention of iron oxide directly from the green synthesis using *Trichoderma harzianum*. After heat treatment (Fe10HT), the analysis for the O 1s orbital assigns the 530.5 eV, 531.7 eV and 532.8 eV signals to metal oxide, C═O and C–O. A considerable energy shift of the signal of metal oxide suggests that Fe was subject to an oxidation process in Fe10HT. Additionally, a new peak appears at 537.0 eV attributed to the Auger Na KLL emission.[18] Overall, the variations in signal intensities in O 1s peaks are attributed to the formation and subsequent loss of superficial functional groups, *e.g.* as CO_2, contained in the sample. To corroborate Fe oxidation and valence, the Fe 2p orbital was measured for both samples, as shown in Fig. 4(d). Here, it is possible to observe the deconvolution in 708.3 eV, 710.6 eV, 712.5 eV and 718.7 eV for Fe10 and 710.6 eV, 711.4 eV, 712.9 eV, 719.0 eV for sample Fe10HT, where a clear shift toward higher binding energies verify the further oxidation of the iron oxide nanomaterials as response to the annealing process. Detailed information regarding the deconvolution for this orbital can be found in Table S3. Although the Fe 2p is a challenging region to analyze due to the multiple oxidation numbers of the Fe element, recent works have pointed out that it is possible to discriminate between iron oxides species.[19] For Fe10 sample, the presence of the first three signals (708.3–712.5) eV can be indicative of Fe_3O_4 formation (FeO/Fe_2O_3) instead of a single phase. The signal in 718.7 eV is associated with the satellite of Fe. On the other hand, for the Fe10HT sample, the signals from 710.6 eV–712.9 eV have been associated with α-Fe_2O_3, which verifies the further oxidation of Fe^{2+} to Fe^{3+}. Therefore, after heat treatment, the phase hematite becomes predominant. The detected α-Fe_2O_3 agrees with the XRD phase identification for this sample. As well as in Fe10, the typical Fe satellite signal was observed at 719.0 eV. XPS analysis of Fe5 and Fe5HT shows the presence of both Fe^{2+} and Fe^{3+} species, indicating a magnetite-based composition for Fe5 and oxidation toward hematite in Fe5HT, consistent with the behavior observed for Fe10 (SI 8, Table S3). The modified Auger parameter (α'), calculated as $\alpha' = E_B$ (Fe $2p_{3/2}$) + E_K (Fe LM2), increases after thermal treatment. Using Fe $2p_{3/2}$ binding energies of 709.9 eV (Fe10) and 710.8 eV (Fe10HT), together with a Fe LM2 kinetic energy of 703.3 eV, α' values of 1413.2 eV and 1414.1 eV were obtained for Fe10 and Fe10HT, respectively. This shift toward higher α' values is consistent with increased Fe(III) character and supports the transformation from a magnetite-based composition to hematite.[20,21]

To study the optical properties of the Fe-based nanomaterials we carried out UV-Visible spectroscopy measurements. To acquire the diffuse absorbance and transmittance measurements, the synthesized nanomaterials were dispersed in ethanol and measured using an integrating sphere module. The absorbance spectra of the Fe10 and Fe10HT samples (Fig. 5a) show an absorption band around 200 nm, which is predominantly associated with organic capping agents, including proteins and metabolites derived from *Trichoderma harzianum*.[22,23] Nevertheless, a minor contribution from trace amounts of hematite may also be present, given reported absorption features of hematite in this wavelength range.[24]

An absorption band centered at approximately 390 nm was observed in the biosynthesized iron oxide nanomaterials, consistent with previous reports on green-synthesized iron oxide nanomaterials.[24–29] Upon heat treatment, this band exhibits a red shift, which is primarily attributed to the phase transformation from magnetite to hematite during annealing, as further supported by XPS analysis.[24,26]In addition, this spectral shift may be partially influenced by particle growth induced by thermal treatment, as larger nanoparticles are known to exhibit absorption at longer wavelengths (SI 2).

Moreover, changes in the surface chemistry associated with heat treatment may also contribute to the observed red shift. Previous studies have suggested that solvent-capping agent interactions can affect the optical response of green-synthesized nanoparticles.[30] In this context, the use of ethanol as a polar protic solvent, combined with thermal modification of the capping biomolecules, may further influence the electronic

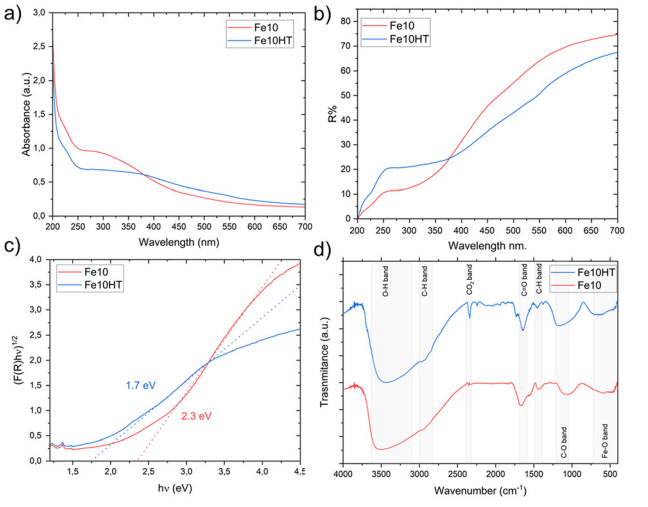

Fig. 5 Optical properties of biosynthesized iron oxide nanomaterials. (a) Absorbance and reflectance spectra of Fe10 and Fe10HT. (c) Tauc plot fitting to determine optical band gap of iron oxide samples. Indirect transition was assumed in the Kubelka–Munk. (d) FTIR absorbance spectra of Fe10 and Fe10HT showing distinct Fe–O vibration modes.

environment of the nanoparticles and contribute to the observed spectral evolution.

Fig. 5(b) presents the diffuse reflectance spectroscopy (DRS) of samples Fe10 and Fe10HT acquired using integrating sphere module. The spectra present the same characteristic bands shown by the absorbance spectra. To further clarify these changes, optical band gap determinations were made using the Tauc plot method, also applying the Kubelka–Munk function ($F(R)$). The results of the band gap interpolation are shown in Fig. 5(c) assuming an indirect transition. Direct transition Tauc plot interpolation is presented in SI 9. Both direct and indirect band gaps decreased as a result of HT process, and their values can be correlated to those of both Fe_2O_3 and Fe_3O_4 iron oxides,[31–35] further corroborating the presence of a mixture of oxides in both Fe10 and Fe10HT samples. The decreases in iron oxide-based materials bandgap in response to an increase in temperature has been reported previously.[36]

To study the functional groups on the surface of the synthesized materials, FTIR measurements were performed for Fe10 and Fe10HT. Fig. 5(d) shows the transmittance spectrum of both samples. From this figure, vibrational bands at 3423 cm^{-1}, 2960 cm^{-1}, 2339 cm^{-1}, 1641 cm^{-1}, 1454 cm^{-1}, 1155 cm^{-1}, and 694 cm^{-1} can be observed, which have been attributed to O–H, C–H, absorbed CO_2, C═O, C–H, and Fe–O vibration modes respectively.

Both Fe10 and Fe10HT samples exhibit a broad band with a maximum absorbance between 3519 cm^{-1} and 3423 cm^{-1} which is reported as O–H stretching vibration associated with the capping agents or with the presence of water molecules in the material. This broad absorption has also been associated with N–H stretching mode in Fe caped nanomaterials by some authors,[37] yet in our case as N content determined by both EDS and XPS is significantly low, it seems unlikely these adsorptions are strongly associated with nitrogen related vibrations. The beforementioned broad band presents two shoulders at 2950–2919 cm^{-1} and 2846 cm^{-1} associated with aliphatic C–H stretching modes. As for the intense peaks around 2339 cm^{-1}, they are associated with asymmetric stretching of CO_2 molecules absorbed in the samples. In 1646 cm^{-1} an intense band appears attributed to C═O stretching which is expected to be related to the capping layer of the nanomaterials. A H–O–H bending band in 1623 cm^{-1} is also reported which can be involved in the red shifting behavior of these bands from Fe10 to Fe10HT samples, as capping layer partially calcinated the dominant vibration transitions from C═O to O–H in this case. In 1452 cm^{-1} C–H the bending band can be associated, while for the broad band from 1182 to 1055 cm^{-1} can be associated with C–O. In this last case the red shifted band in Fe10 can be correlated to C–O–C band,[28] suggesting thermal degradation produces C mass loss as CO_2 gas is generated from the oxidation process. These bands observed are due to possible presence of metabolites and proteins acting as capping agents, essential for the redox process and nanoparticles stabilization of iron oxide NPs. In fact, Gallo *et al.*, characterized, using SDS-PAGE, several metabolites and proteins contained in *Trichoderma harzianum* and can be responsible for the formation of iron oxide NPs,[4] *e.g.* oxidoreductases. Finally, the broad band appearing below 700 cm^{-1} has been previously associated with Fe–O vibration mode further confirming the formation of iron oxide nanomaterials by green synthetic process.

We proceeded to evaluate the biostimulant effect of the biosynthesized nanoparticles (both Fe5 and Fe10 without heat treatment) on *Trichoderma harzianum* against pathogens grown. At 100 ppm NPs supplementation of the PDA culture media, both Fe5 and Fe10 enhanced sporulation and induced darker pigmentation compared to the control (PDA culture media without iron oxide NPs), which exhibited the lowest conidial formation (Fig. 6(a)). Notably, Fe10 promoted the most intense conidial formation, suggesting that NPs supplementation accelerates fungal reproductive processes. These findings indicate that iron oxide nanoparticles act as growth promoters, consistent with previous studies showing that concentrations below 500 mg L^{-1} favor fungal growth and sporulation.[38] Similar tolerance to iron oxide nanoparticles has been reported in *Trichoderma atroviride* and *Trichoderma asperellum* at up to 100 ppm, with no adverse impact on growth,[39] a behavior attributed to the ability of *T. harzianum* to withstand high metal concentrations.[40]

Growth kinetics revealed that Fe10 accelerated mycelial expansion and sporulation from the early stages of culture, with marked morphological differences (Fig. 6(b)). After 24 h, *T. harzianum* + Fe10 covered 3.97 cm^2 compared to 2.5 cm^2 in the control, and by day 2 both treatments fully colonized the Petri dish. However, from day 3 onwards, Fe10 promoted denser yellow mycelium, while the control displayed patchy white growth. By day 4, Fe10-treated cultures exhibited pronounced pigmentation and abundant sporulation, covering the dish completely, whereas sporulation in the control remained limited. At days 6–7, both treatments formed green conidia, but sporulation was more intense in Fe10, particularly at the margins. These results demonstrate that iron oxide

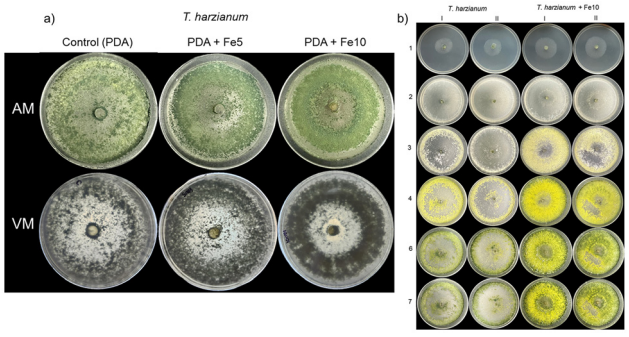

Fig. 6 (a) Photographs of aerial mycelium (AM) and vegetative mycelium (VM) of *Trichoderma harzianum* grown on PDA (control), PDA + Fe5 (100 ppm), and PDA + Fe10 (100 ppm) after seven days of incubation. (b) Photographs of aerial mycelium showing *Trichoderma harzianum* growth from PDA and *T. harzianum* + Fe10 over seven days of incubation. Growth is presented with single replicates (I, II) for both conditions.

nanoparticles accelerated reproductive development, aligning with Bilesky-José *et al.*,[41] who reported faster growth kinetics and greater conidial density in nanoparticle-supplemented *T. harzianum*.

In dual culture assays, Fe5 and Fe10 consistently improved *T. harzianum* antagonism against *Fusarium oxysporum*, *Fusarium verticillioides*, and *Phytophthora infestans* (Fig. 7). In all cases, nanoparticle supplementation reduced pathogen competitiveness, altered pathogen mycelial morphology, and advanced the onset of antagonism compared with controls. In confrontation with *F. oxysporum*, the control was classified as antagonism level three (no dominance), whereas Fe5 and Fe10 treatments shifted the interaction to level two, with *T. harzianum* colonizing two-thirds of the plate and producing abundant green conidia. The pathogen, in contrast, developed darker vegetative mycelium and restricted growth. Against *F. verticillioides*, the control also recorded level three antagonism, with *T. harzianum* overgrowth occurring only after day 10. In Fe5 and Fe10 enriched treatments, however, pathogen darkening occurred as early as day 3, while *T. harzianum* developed dense green mycelium by day 7 and colonized two-thirds of the dish by day 10, resulting in level two antagonism. With *P. infestans*, the pathogen initially dominated, occupying two-thirds of the dish by day 3. In the control, *T. harzianum* displayed limited yellow mycelium at day 7 and overgrew the pathogen only by day 10. In contrast, Fe5 and Fe10 accelerated the antagonistic response, with *T. harzianum* colonizing over *P. infestans* by day 7, achieving level two antagonism. These findings are consistent with previous studies demonstrating improved antagonism of *T. harzianum* in the presence of iron oxide nanoparticles.[41] To isolate nanoparticle-specific effects, control experiments were performed using ferrous acetate at the same iron concentration in PDA. As shown in Fig. S10, no significant differences were observed between the PDA control and PDA supplemented with ferrous acetate, whereas the Fe5 and Fe10 materials induced a pronounced stimulation of the antagonistic response of *T. harzianum*.

Overall, the results demonstrate that biosynthesized iron oxide nanoparticles not only stimulate the growth and sporulation of *T. harzianum* but also potentiate its antagonistic capacity against key phytopathogens. The dual role of iron oxide nanoparticles, as metabolic stimulants and biocontrol enhancers, suggests that their application as promising co-adjuvants in sustainable agricultural strategies, improving the efficacy of *Trichoderma*-based biocontrol while maintaining compatibility with soil microbiota.[39]

Fig. 8 schematically illustrates the proposed mechanism by which *Trichoderma harzianum* induces redox reactions that convert iron(II) acetate into iron oxide nanoparticles. According to the mechanism proposed by Begum *et al.*,[26] Fe^{2+} ions originating from the precursor salt are initially reduced to transient Fe^{0} species by metabolites and proteins secreted by *Trichoderma harzianum*, which act as biological reducing agents. Under the acidic conditions of the system, these zero-valent iron species are readily re-oxidized to Fe^{2+} and Fe^{3+}, leading to the formation of mixed-valence iron oxide nanostructures, as corroborated by XPS analysis. Simultaneously, fungal metabolites absorb onto the nanoparticle surface, acting as capping agents that stabilize the nanostructures, limit long-range crystallographic order prior to thermal treatment and subsequently serve as biostimulants that enhance *T. harzianum* growth and its antagonistic activity against agriculturally relevant phytopathogens. Table 2 summarizes previous studies on the biosynthesis of iron oxides mediated by *T. harzianum* species. Across all reports, this fungus consistently demonstrates the ability to form iron oxide nanoparticles

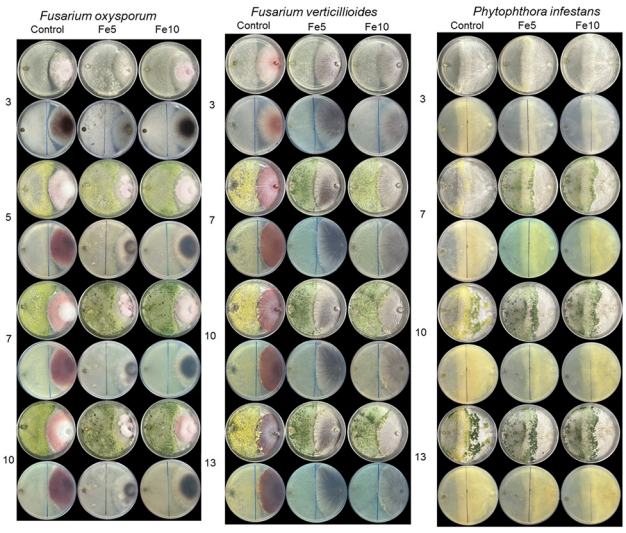

Fig. 7 Antagonistic activity of *Trichoderma harzianum* on PDA medium (control) and on PDA supplemented with Fe5 or Fe10 against *Fusarium oxysporum*, *Fusarium verticillioides*, and *Phytophthora infestans*. Treatments were evaluated for 10 days (*F. oxysporum*) and 13 days (*F. verticillioides* and *P. infestans*).

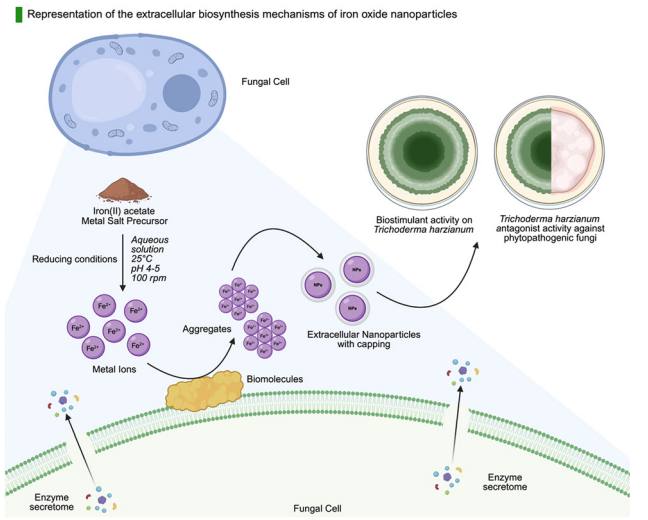

Fig. 8 Schema of biosynthesis of iron oxide NPs using *T. harzianum* and their posterior application as both biostimulant agent and phytopathogen control enhancer. Created with BioRender.

Table 2 Comparison of different biosynthesized iron oxide nanoparticles using *Trichoderma* sp. fungi

Fungus	Metallic precursor	Biosynthesized material	Ref.
Trichoderma harzianum	Iron chloride	α-Fe_2O_3	41
Trichoderma harzianum	Ferrous sulphate	FeO	4
Trichoderma harzianum	Iron chloride	α-Fe_2O_3	42
Trichoderma harzianum	Iron chloride	Fe_2O_3	43
Trichoderma asperellum	Iron chloride	Fe_2O_3	44
Trichoderma harzianum	Ferrous acetate	Fe_2O_3/Fe_3O_4 NPS	This work

regardless of the precursor used, while the resulting nano or microstructures significantly enhance its growth and antifungal performance. However, at the chemical and structural level, the precursor type strongly influences particle morphology and size. In the present study, the biosynthetic strategy led to the formation of smaller nanostructures compared with those previously reported, highlighting the efficiency of the proposed synthesis route.

4. Conclusions

The biosynthesis of Fe-based nanomaterials using *Trichoderma harzianum* enabled the formation of hybrid micro-nanostructures with controllable morphology and composition. SEM and AFM analyses revealed a clear correlation between precursor concentration and particle architecture: while 5 mM (Fe5) precursors yielded smaller microstructures decorated with homogeneous quasi-spherical nanoparticles, the 10 mM (Fe10) condition promoted denser surface coverage, increased roughness, and agglomeration effects. TEM analysis confirmed the presence of nanoscale aggregates and highlighted the amorphous character of the as-synthesized samples, which transformed into crystalline α-Fe_2O_3 (hematite) after post-synthesis calcination. Structural rearrangement upon thermal treatment was validated by SAED, XRD, and XPS, evidencing oxidation from Fe_3O_4 (Fe^{2+}/Fe^{3+} mixed phases) into Fe_2O_3 (hematite) Elemental and surface analyses further demonstrated the gradual removal of biologically derived capping agents, as volatile species. Finally, optical spectroscopy confirms the obtention iron oxide NPs, as reflected by characteristic band gap features, with thermal treatment inducing redshifts and narrowing of the optical band gap. Altogether, these findings demonstrate the feasibility of *Trichoderma harzianum* to synthesize iron oxide nanoparticles using a green approach.

The biological assays demonstrated that biosynthesized iron oxide nanoparticles (both Fe5 and Fe10) act as effective biostimulants for *Trichoderma harzianum*, enhancing mycelial development, sporulation, and conidial pigmentation without inhibitory effects. Growth kinetics revealed accelerated colonization and reproductive structure formation of *Trichoderma harzianum*, with superior enhancement using Fe10 sample, compared with the control. Moreover, dual culture experiments confirmed that Fe5 and Fe10 improved the antagonistic capacity of *T. harzianum* against *Fusarium oxysporum*, *Fusarium verticillioides*, and *Phytophthora infestans*, restricting pathogen growth. These results highlight the synergistic effect of the biosynthesized iron oxide nanoparticles to increase the activity of *Trichoderma*-based as biological control agent, promoting new strategies for sustainable agriculture.

Author contributions

EAJ: methodology, investigation, data analysis, and writing – original draft & review. AARR: investigation, data curation, and writing – original draft. AGM: methodology, investigation, data analysis, editing and writing – original draft & review. ARVO: conceptualization and funding acquisition. VBKY: writing – review & editing. SO: writing – review & editing. OAC: conceptualization. SA: funding acquisition, writing – review & editing, and project administration.

Conflicts of interest

There are no conflicts to declare.

Data availability

All the data presented in the article is uploaded in the ZENODO repository https://doi.org/10.5281/zenodo.17392500.

Supplementary information (SI) is available. See DOI: https://doi.org/10.1039/d5nr04745e.

Acknowledgements

The authors acknowledge the financial support from the Mexican Council of Science, Humanities, Technology and Innovation (postdoctoral fellowship CVU 770372), the Fondo Hidalgo (No. DDCTI/FH-DCI-052), the Research Council of Finland decision No. 363120 (pH2) and Profi 352788 (H2FUTURE) projects. We thank the Colegio de Postgraduados Campus Montecillo for the strains of phytopathogens used in this study. The Center of Materials Analysis (CMA) at the University of Oulu is acknowledged for materials characteriztions.

References

1 Y. R. Hasan, F. W. Faizal Wong, S. E. Ashari, M. Halim and R. Mohamad, *Appl. Microbiol. Biotechnol.*, 2025, **109**, 202.
2 H. J. Fatih, M. Ashengroph, A. Sharifi and M. M. Zorab, *BMC Microbiol.*, 2024, **24**, 535.
3 S. Armenta, E. Armenta Jaime, A. Galdámez Martínez, Á. A. Rivera Román, V. Rodríguez Lugo and O. Arce Cervantes, *Tóp. Investig. Cienc. Tierra Mater.*, 2024, **11**, 66–75.

4 M. B. Gallo, A. N. Bader, A. Torres-Nicolini, V. A. Alvarez and V. F. Consolo, *Sci. Rep.*, 2025, **15**, 3252.
5 G. M. Herrera Pérez, L. E. Castellano and C. A. Ramírez Valdespino, *J. Fungi*, 2024, **10**, 443.
6 Y. Shao, S. Gu, H. Peng, L. Zhang, S. Li, R. L. Berendsen, T. Yang, C. Dong, Z. Wei, Y. Xu and Q. Shen, *npj Biofilms Microbiomes*, 2025, **11**, 56.
7 D. K. Bell, *Phytopathology*, 1982, **72**, 379.
8 E. Armenta-Jaime, J. Molina-González, K. P. Salas-Martin, R. Fan, L.-Y. Chang, J.-L. Chen, P. Steadman, H. Desirena-Enrriquez, A. Dutt, P. Olalde-Velasco and S. E. Castillo-Blum, *Phys. Chem. Chem. Phys.*, 2023, **25**, 20308–20319.
9 M. Klinger, *J. Appl. Crystallogr.*, 2017, **50**, 1226–1234.
10 A. L. Patterson, *Phys. Rev.*, 1939, **56**, 978–982.
11 G. Greczynski and L. Hultman, *Appl. Surf. Sci.*, 2022, **606**, 154855.
12 F. B. Effenberger, M. A. Sulca, M. T. Machini, R. A. Couto, P. K. Kiyohara, G. Machado and L. M. Rossi, *J. Nanopart. Res.*, 2014, **16**, 2588.
13 M. Skorupska, P. Kamedulski, J. P. Lukaszewicz and A. Ilnicka, *Nanomaterials*, 2021, **11**, 1–13.
14 B. V. Crist, *J. Electron Spectrosc. Relat. Phenom.*, 2019, **231**, 75–87.
15 X.-Z. Song, Y.-H. Zhao, F. Zhang, J.-C. Ni, Z. Zhang, Z. Tan, X.-F. Wang and Y. Li, *Nanomaterials*, 2022, **12**, 3972.
16 Y. Shi, Y. Yu, Y. Liang, Y. Du and B. Zhang, *Angew. Chem., Int. Ed.*, 2019, **58**, 3769–3773.
17 G. Deng, T. Wang, A. A. Alshehri, K. A. Alzahrani, Y. Wang, H. Ye, Y. Luo and X. Sun, *J. Mater. Chem. A*, 2019, **7**, 21674–21677.
18 L. Chen, B. Kishore, M. Walker, C. E. J. Dancer and E. Kendrick, *Chem. Commun.*, 2020, **56**, 11609–11612.
19 M. C. Biesinger, B. P. Payne, A. P. Grosvenor, L. W. M. Lau, A. R. Gerson and R. St. C. Smart, *Appl. Surf. Sci.*, 2011, **257**, 2717–2730.
20 B. Lesiak, N. Rangam, P. Jiricek, I. Gordeev, J. Tóth, L. Kövér, M. Mohai and P. Borowicz, *Front. Chem.*, 2019, **7**, 642.
21 P. Kumar, M. C. Mathpal, G. K. Inwati, S. Kumar, M.-M. Duvenhage, W. D. Roos and H. C. Swart, *Magnetochemistry*, 2023, **9**, 20.
22 A. Staropoli, G. Iacomino, P. De Cicco, S. L. Woo, L. Di Costanzo and F. Vinale, *Chem. Biol. Technol. Agric.*, 2023, **10**, 28.
23 A. Hugar, M. Rudrappa and S. Nayaka, *Microb. Pathog.*, 2025, **204**, 107606.
24 A. A. Qureshi, S. Javed, H. M. A. Javed, M. Jamshaid, U. Ali and M. A. Akram, *Nanomaterials*, 2022, **12**, 1635.
25 F. Li, Z. Yu, L. Zhao and T. Xue, *RSC Adv.*, 2016, **6**, 10352–10357.
26 S. K. Begum, D. Shabnam, N. Haque, M. J. Alam, J. Ferdous, U. J. B. Nur, K. Fatema, R. J. Shabiha, R. J. Clarke, P. Chowdhury and Md. N. Uddin, *Sci. Rep.*, 2025, **15**, 36465.
27 H. Y. El-Kassas, M. A. Aly-Eldeen and S. M. Gharib, *Acta Oceanol. Sin.*, 2016, **35**, 89–98.
28 E. S. Madivoli, P. G. Kareru, E. G. Maina, A. O. Nyabola, S. I. Wanakai and J. O. Nyang'au, *SN Appl. Sci.*, 2019, **1**, 1–11.
29 B. Kumar, K. Smita, L. Cumbal and A. Debut, *J. Saudi Chem. Soc.*, 2014, **18**, 364–369.
30 D. Farhanian, G. De Crescenzo and J. R. Tavares, *Sci. Rep.*, 2018, **8**, 1–11.
31 G. J. Meyer, J. M. Gardner, S. Kim and P. C. Searson, *J. Nanomater.*, 2011, 737812.
32 H. El Ghandoor, H. M. Zidan, M. M. H. Khalil and M. I. M. Ismail, *Int. J. Electrochem. Sci.*, 2012, **7**, 5734–5745.
33 I. Mimouni, A. Bouziani, Y. Naciri, M. Boujnah, M. A. El Belghiti and M. El Azzouzi, *Environ. Sci. Pollut. Res.*, 2022, **29**, 7984–7996.
34 T. Saragi, B. L. Depi, S. Butarbutar, B. Permana and Risdiana, *J. Phys.: Conf. Ser.*, 2018, **1013**, 012190.
35 S. Delice, M. Isik and N. M. Gasanly, *Chem. Phys. Lett.*, 2024, **840**, 141139.
36 S. A. Kadam, G. T. Phan, D. Van Pham, R. A. Patil, C. C. Lai, Y. R. Chen, Y. Liou and Y. R. Ma, *Nanoscale Adv.*, 2021, **3**, 5581–5588.
37 S. Kumar, H. Kaur, H. Kaur, I. Kaur, K. Dharamvir and L. M. Bharadwaj, *J. Mater. Sci.*, 2012, **47**, 1489–1496.
38 Z. Shi, Y. Zhao, S. Liu, Y. Wang and Q. Yu, *Molecules*, 2022, **27**, 5840.
39 P. Amézaga-Madrid, E. García-Mireles, E. García-Meléndez, A. Vázquez-Ramírez and C. A. Ramírez-Valdespino, *Chemosphere*, 2025, **371**, 144047.
40 C. A. Ramírez-Valdespino and E. Orrantia-Borunda, *Frontiers in Fungal Biology*, 2021, **2**, 764675.
41 N. Bilesky-José, C. Maruyama, T. Germano-Costa, E. Campos, L. Carvalho, R. Grillo, L. F. Fraceto and R. de Lima, *ACS Sustainable Chem. Eng.*, 2021, **9**, 1669–1683.
42 S. Sharma, P. Kumari, M. Shandilya, S. Thakur, K. Perveen, I. Sheikh, Z. Ahmed, R. Sayyed and A. Mastinu, *J. Basic Microbiol.*, 2025, **65**, e2400613.
43 M. Akbar, U. Haroon, M. Ali, K. Tahir, H. J. Chaudhary and M. F. H. Munis, *J. Appl. Microbiol.*, 2022, **132**, 3735–3745.
44 S. Mahanty, M. Bakshi, S. Ghosh, S. Chatterjee, S. Bhattacharyya, P. Das, S. Das and P. Chaudhuri, *Bionanoscience*, 2019, **9**, 637–651.